

Research Article

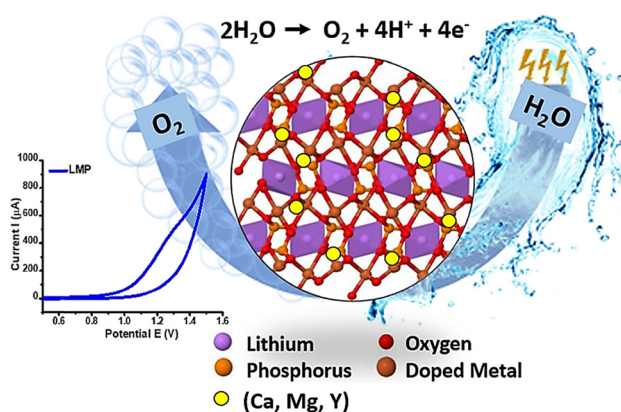
Mehwish Huma Nasir, Hajira Niaz, Naila Yunus, Urooj Ali, Safia Khan, Tehmeena Maryum Butt, Hina Naeem, Hu Li, Mohamed A. Habila, and Naveed Kausar Janjua*

Calcium-, magnesium-, and yttrium-doped lithium nickel phosphate nanomaterials as high-performance catalysts for electrochemical water oxidation reaction

<https://doi.org/10.1515/ntrev-2023-0166>

received October 10, 2023; accepted November 16, 2023

Abstract: Electrochemical water oxidation reaction (WOR) lies among the most forthcoming approaches toward eco-conscious manufacturing of green hydrogen owing to its environmental favors and high energy density values. Its vast commoditization is restricted by high-efficiency and inexpensive catalysts that are extensively under constant research. Herein, calcium, magnesium, and yttrium doped lithium nickel phosphate olivines ($\text{LiNi}_{1-x}\text{M}_x\text{PO}$, LNMP; $x = 0.1-0.9$; $\text{M} = \text{Ca}^{2+}$, Mg^{2+} , and Y^{3+}) were synthesized *via* non-aqueous sol-gel method and explored for catalytic WOR. Lithium nickel phosphates (LNP) and compositions were characterized *via* Fourier transform infrared, scanning electron microscopy, X-ray diffraction, and energy dispersive X-ray diffraction techniques for the structural and morphological analyses. Glassy carbon electrode altered with the LNMPs when studied in a standard redox system of 5 mM KMnO_4 , displayed that yttrium doped LNP, *i.e.* LNYP-3



Graphical abstract: Electrochemical water oxidation over high-efficiency (Ca, Mg, or Y) doped lithium metal (Ni) phosphate electrocatalysts

exhibits the highest active surface area (0.0050 cm^2) displaying the lowest average crystallite size (D_{avg}) *i.e.* $\sim 7 \text{ nm}$. Electrocatalytic behavior monitored in KOH showed that LNMP-2 offers the highest rate constant “ k^0 ,” value, *i.e.* $3.9 \times 10^{-2} \text{ cm s}^{-1}$ and the largest diffusion coefficient “ D^0 ,” *i.e.* $5.2 \times 10^{-5} \text{ cm}^2 \text{ s}^{-1}$. Kinetic and thermodynamic parameters demonstrated the facilitated electron transfer and electrocatalytic properties of proposed nanomaterials. Water oxidation peak current density values were indicative of the robust catalysis and facilitated water oxidation process besides lowering the Faradic onset potential signifying the transformation of less LNP into more conductive LNMP toward water oxidation.

Keywords: lithium nickel phosphate, Ca, Mg, Y-doped LNP, nanomaterial, sol-gel method, electrocatalytic water oxidation, sustainable development, electrocatalysts

Nomenclature

LNP lithium nickel phosphate
LNMP lithium nickel metal phosphate

* **Corresponding author: Naveed Kausar Janjua**, Department of Chemistry, Quaid-i-Azam University, Islamabad, 45320, Pakistan, e-mail: nkjanjua@qau.edu.pk

Mehwish Huma Nasir: Department of Chemistry, Quaid-i-Azam University, Islamabad, 45320, Pakistan; Department of Chemistry, Rawalpindi Women University, Rawalpindi, 46000, Pakistan

Hajira Niaz, Naila Yunus, Urooj Ali, Tehmeena Maryum Butt: Department of Chemistry, Quaid-i-Azam University, Islamabad, 45320, Pakistan

Safia Khan: Shandong Technology Centre of Nanodevices and Integration, School of Microelectronics, Shandong University, Jinan, 250101, China

Hina Naeem: Department of Chemistry, Rawalpindi Women University, Rawalpindi, 46000, Pakistan

Hu Li: Ångström Laboratory, Department of Materials Science and Engineering, Uppsala University, 75121, Uppsala, Sweden

Mohamed A. Habila: Department of Chemistry, College of Science, King Saud University, Riyadh, 11451, Saudi Arabia

CV	cyclic voltammetry
ASA	active surface area
WOR	water oxidation reaction
DMFC	direct methanol fuel cell
ORR	oxygen reduction reaction
HER	hydrogen evolution reaction
XRD	X-ray diffraction
FTIR	Fourier transform infrared
SEM	scanning electron microscopy
EDS	energy dispersive spectroscopy
GCE	glassy carbon electrode
ΔG	change in Gibbs free energy
ΔH	change in enthalpy
ΔS	change in entropy
D_{avg}	average crystallite size
D^0	diffusion coefficient
k^0	heterogeneous rate constant
m_T	mass transport coefficient

1 Introduction

Undue consumption of fossil fuels is a major contributing factor that has increased pollution and greenhouse gases that led to global warming and ozone depletion by emitting hazardous carbon compounds as major concerned outcomes [1,2]. To overcome these drawbacks, efficient and green energy production technology is necessitated to meet the decarbonized energy goals, thereby minimizing global climate changes [2,3]. Green energy includes clean power sources, *e.g.* solar power, biomass, wind, hydro-power, and geothermal. Green energy technology is a collaborative strategy that combines conventional fossil fuel systems and updated renewable technologies in terms of accessibility, efficiency, energy security, equity, and economic sustainability [4,5]. Keeping in view the significance of clean energy and low carbon environment, findings of alternative energy resources are key research areas nowadays [6]. Pollution-free, clean, and green energy is produced by renewable energy sources but for sustainable energy supply, electrochemical energy is the economical storage system [7]. Electrochemical methods like hydrogen evolution reaction (HER), oxygen evolution reaction (OER), and oxygen reduction reaction (ORR) are used for the production of viable energy [8]. HER and OER in alkaline media are usually slow reactions that need the use of an electrocatalyst to increase their efficiency and potentiality. Electrocatalysis takes place at the electrode-solution interface where the electrode is modified by a catalyst at its surface [9,10]. The development of nonprecious metal-

based electrocatalysts and new electrolytic systems toward water oxidation is an active research area that still needs further improvement and perfection [11,12]. Among multiple energy conversion means, direct methanol fuel cell (DMFC) possesses various advantages including the adoption of nonprecious electrocatalysts such as CeO_2 , $\text{NiCu-CO}_2\text{O}_4$, green synthesized catalysts, zeolite base catalysts, algal based catalysts, and SeO_2 [13,14]. Risks of corrosion of carbon and catalysts are predominantly diminished. The performance of alkaline DMFC mainly depends on the electrocatalytic responses of electrocatalysts at the surface of the electrode, electrode/electrolyte interface, and the ion and electron transfer rate in the electrode [15,16]. So, the development of novel electrocatalysts with enhanced stability and electroactivity is a prerequisite for such high-efficiency conversion technologies [17]. Various electrocatalysts for water oxidation include perovskites, halides, selenides, layered double hydroxides and nickel, cobalt-based oxide, algal membranes, each having their recompenses and drawbacks. Perovskite oxides show the deviation from the ideal stoichiometry due to the substitution of A/B-sites leading to electrochemical stability [18]. Doping and modifications in material alter the stoichiometry and create defects in the crystal structure of the material. A larger number of defect insertion points offer more oxygen vacancies and hence the active sites [19]. Doping in A-site with alkaline metal ions and B-site with transition metal ions creates defects in the arrangement of crystal [20]. In water oxidation, oxygen is produced OER, and reduction reaction produces a hydrogen evolution reaction (HER). Water oxidation is a single-step reaction due to which large overpotentials are produced, and to overcome this, large overpotential efficient electrocatalysts are needed. Overpotential is the difference in equilibrium/thermodynamic potential of a reaction and the real potential where the catalyst actually initiates the reaction at a specific current under control conditions. Low-overpotential WOR is required for progressed energy conversion technology [21,22]. The best catalysts so far used for OER are Pt and Ir oxide but these are expensive and less abundant [23].

Nickel-incorporated nanomaterials, being used in supercapacitors, electrocatalysts, battery materials and sensors, have earned particular emphasis from researchers owing to their abundance, low cost, and environment friendliness [24,25]. Owing to its large redox potentials *i.e.* $>4.5\text{ V vs Li}^+/\text{Li}$, high energy and voltage, nickel-derived olivine (LNP) has acquired greater emphasis among the olivine phosphates (800 W h g^{-1}) [26]. Olivine edifices are constructed with MO_6 sharing octahedral sides and tetrahedral anions of phosphates at corners where octahedral holes are exchanged by lithium ions [27]. LiNiPO_4 as an electrocatalyst possesses some

general properties such as high thermal stability, durable potentials, unique electrochemical properties, inexpensive, environmentally friendly, and excellent cycling performance [28,29]. The drawback of WOR is the reversibility of reaction, by recombination of electrons and holes which may slow down the reaction. A sacrificial agent is used for preventing this drawback which acts as an electron donor molecule by reacting with the holes. Through this method, the production of O_2 and H_2 increased by using methanol, glucose, ethanol, cyanide, and formaldehyde as a sacrificial agent [30]. Methanol is reported as a sacrificing agent/facilitating agent/co-catalyst for WOR by our group that boosted the charge transfer through the electrode and decreased the onset potential [31]. Sacrificial agents are basically the electron donors or hole scavengers that boost up the H_2 production by anchoring on the electrocatalyst's surface [32]. A co-catalyst involved mechanism is also an uphill WOR; however, the onset potential is comparatively less [33].

In this work, a cost-effective non-aqueous sol–gel synthesis approach is adapted for the preparation of LNP and PNMP ($LiNi_{1-x}M_xPO_4$) where M can be Mg, Ca, and Y in the perovskite structure. Physiochemical characterization is accomplished via XRD, FTIR, SEM, EDS, and CV for investigating the phase purity, particle size, surface area, and electronic properties. The voltammetric profile is established in KOH as the electrolyte because protons produced in WOR can be facilely removed in an alkaline medium, thereby restoring the catalyst's original pristine state [34]. WOR is studied on different metal-doped $LiNiPO_4$ in KOH using glucose as the facilitating agent for the first time.

2 Experimental section

2.1 Materials

Precursors include metal nitrate of lithium ($LiNO_3 \cdot 3H_2O$), nickel ($Ni(NO_3)_2 \cdot 6H_2O$), magnesium ($Mg(NO_3)_2 \cdot 3H_2O$), Calcium ($Ca(NO_3)_2 \cdot 4H_2O$), yttrium ($Y(NO_3)_3 \cdot 6H_2O$), phosphoric acid (H_3PO_4), and ethylene glycol. All the chemicals are bought from Sigma–Aldrich. Solutions were prepared in deionized water.

2.2 Synthesis

Non-aqueous wet-chemical sol–gel method is employed to manufacture the olivine orthophosphate, $LiNiPO_4$, and metal-doped (Ca, Mg, and Y) lithium nickel phosphate composites [35,36]. The preparation technique comprises of

heating of metalloorganic gel precursors. The non-aqueous mixture was organized by stoichiometric ratio of 1:1:1 of the lithium and nickel nitrate in ethylene glycol while the (H_3PO_4) was added dropwise under the continuous stirring of the solution for 2 h at $200^\circ C$. The obtained gel precursors were heated to produce the powder of nanomaterials. Synthesized powders were calcined in the furnace at $850^\circ C$ temperature for 12 h under air atmosphere and cooled at room temperature. For the synthesis of the doped composition of lithium nickel phosphate, a stoichiometric amount of the magnesium, calcium, yttrium nitrate, and nickel nitrate were added to obtain the metal-doped lithium nickel phosphate where mole % of dopants ranges 0–9%.

Furthermore, mechanical ball milling was performed for all calcined powders using zirconia balls (100 g) of different diameters. Zirconia balls are used for their large mass/volume ratio; producing course-sized particles of catalyst powder [37,38]. It is a grinding phenomenon utilized to produce a homogeneous particle size of the sample [39,40]. Milling media (acetone) are filled according to the specific ratio of the sample and ball, which means the mass of the ball is one-fourth times greater than the weight of the samples [41]. Acetone is preferred in dry-milling as the material does not stick to the balls and can be isolated feasibly [42]. The ball milling was sustained for 2 h under 300 rpm, and afterward, the mixture was placed in the oven for 5 h for drying. Sample simplified representation into codes is presented in Table 1.

2.3 Physical characterization

Different analytical techniques were utilized for investigating the physical and chemical composition of synthesized materials. For the determination of the crystal assembly and phase concentration of prepared materials, powder XRD (D5005 diffractometer, Siemens) was pragmatized. All the XRD measurements were done with a sol X detector

Table 1: Coding of samples into simpler abbreviations $LiNi_{1-x}M_xPO_4$ [M = Mg, Ca, and Y]

Mol% of dopants	Samples codes	Chemical formula
0	LNP	$LiNiPO_4$
1	LNMP-1	$LiNi_{0.99}M_{0.01}PO_4$
3	LNMP-2	$LiNi_{0.97}M_{0.03}PO_4$
5	LNMP-3	$LiNi_{0.95}M_{0.05}PO_4$
7	LNMP-4	$LiNi_{0.93}M_{0.07}PO_4$
9	LNMP-5	$LiNi_{0.91}M_{0.09}PO_4$

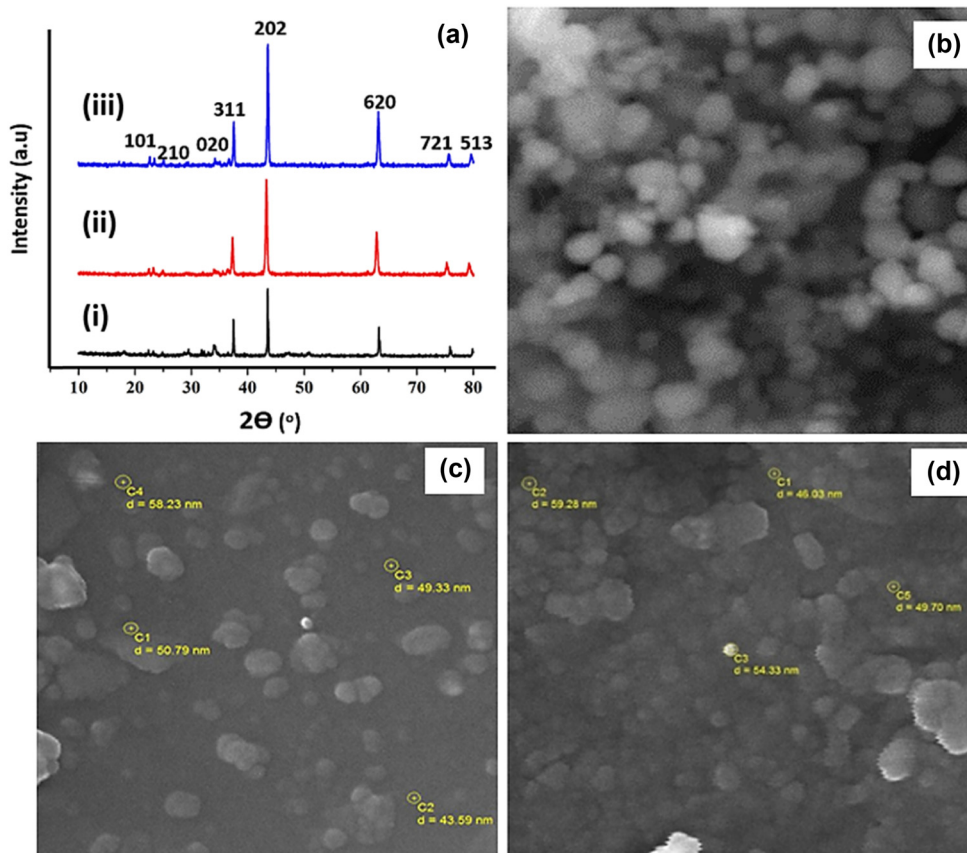


Figure 1: (a) XRD spectra of LNCP-1 (i), LNMP-2 (ii), and LNYP-3 (iii), respectively. (b) SEM micrographs of LNCP-1, (c) LNMP-2, and (d) LNYP-3.

employing a Cu α radiation source with the 1.54 Å wavelength in the 10°–80° range for a widespread and deep understanding of the physical picture of material at the ambient temperature. FTIR analysis was carried out to measure the intensity of infrared radiation as a function of wavelength. A small portion of the sample was sandwiched in KBr for FTIR evaluation, and spectra were then collected as an average of five examinations by means of the OPUS Software Package for data gaining. SEM has been accomplished to obtain the texture and particle size of composites. A field-emission scanning electron microscope (Supra55. Zeiss) with a 10 kV quickening voltage was set to obtain micrographs for the SEM. Electrochemical Gamry 1000 interface instrument was used for the electroanalytical analysis of materials through cyclic voltammetry.

2.4 Electrode fabrication and electrochemical characterization

For electrochemical application, a three-electrode cell assembly is used which consists of three electrodes, *i.e.* glassy carbon

electrode (GCE) as the working electrode, silver wire as the counter electrode, and Ag/AgCl as the reference electrode. GCE was modified by a conventional drop-casting technique [31,43]. In this technique, the working electrode was polished on the felt paper by using an alumina slurry and then rinsed with deionized water before the modification. Polishing and ultrasonication are completed in ethanol for 2 min for the removal of any impurity present on the electrode surface. The electrode surface was wet with 2 μ L of ethanol and 0.1 mg of the synthesized powder was placed on it, resulting in the drop-casting 2 μ L 0.5% of Nafion (co-polymer of sulfonated tetrafluoroethylene) acting as a binder [43]. All produced nanomaterials were investigated to examine their behavior toward water oxidation in 0.1 and 0.5 M KOH used as a supporting electrolyte, and 0.05 (3.2 μ M) glucose was also utilized as a sacrificial agent. The full potential range voltammogram showed only an OER peak, and no other peak appeared. Thus, it is suggested that a short window range (0–1.5, 1.6) is better for the further working of the catalyst. Cyclic voltammetry is implicated as the analytical tool to investigate the electrochemical potentials of the prepared olivine materials toward water oxidation reaction.

Table 2: Calculated crystallite sizes and EDX analysis of LNP and its Ca-, Mg-, and Y-doped analogues

Sample	D_{avg} (nm)	wt% of O _(exp)	wt% of P _(exp)	wt% of Ni _(exp)	wt% of dopant _(exp)	wt% of dopant _(Theo)
LNP	9.2	62.6	15.6	21.8	0.00	0.00
LNMP-2	9.0	44.6	20.2	33.8	1.24	1.38
LNCP-1	9.2	46.7	23.7	23.7	0.95	0.99

3 Results and discussion

Material's physiochemical characterization and catalytic studies are presented in this section. To analyze the high-efficiency LNPs, deep-rooted material investigation was carried out earlier than the electroanalytical research. To understand the simultaneous analysis of electrode engineering and material properties, synthesized materials were tested electrochemically. LNPs were synthesized under an air atmosphere at 850°C and ball milled for smooth narration. Electrochemical tests were first performed with LiNiPO₄ powder. For the authentication of doping in the prepared sample and to study the accuracy of the structural features, morphology, and thermal stability of the samples, various experimental techniques were also employed. The redox and electrocatalytic properties of all the prepared samples were examined via CV. The crystal structure of electrode materials was studied via XRD. Diffraction patterns for LNP and its Ca-, Mg-, and Y-doped analogues are shown in Figure 1(a). Peaks clearly designated the orthorhombic structure of olivine with the Pnma phase group and displayed the desired agreement with reference card JCPDS card No. 81-1528 [44]. There are no peak shifts observed by the addition of external new metal as its content percentage is in traces. However, the peak intensity is altered suggesting the formation of crystal structure and extent of crystallinity. The basic structure is not significantly changed but the catalytic efficiency is enhanced by defect formations. High-intensity peaks evidences the decidedly crystalline morphology, whereas the peaks shown by ball-milled samples exposed great widths owing to smaller crystallite sizes calculated using Debye Scherrer equation shown by equation (1) [45].

$$D_{\text{avg}} = k \lambda / \beta \cos \theta. \quad (1)$$

Peak positions are not altered, hence signifying the integrity of crystalline structure. D_{avg} of LNP and its Ca-, Mg-, and Y-doped analogues are represented in Table 1, respectively. The range of D_{avg} is from 9.24 to 10.5, 9.04 to 9.58, and 7.0 to 11.3 nm for Ca-, Mg-, and Y-doped materials, respectively. Morphological studies of the samples have been accomplished via SEM, and the micrographs are shown in Figure 1(b–d) where particles preserved the distinguishable grain boundaries and smooth surface structure. Spherical

particles increase the surface area of the interface, however, show the agglomeration of the particles due to their smooth and steamy nature. Moreover, the elemental composition of LNP and its doped analogues were expounded by EDX as given in Table 2, and respective spectra are displayed in Figure 2. The determined elemental composition is about similar to the predictable ratios of elements, hence suggesting it is an adaptable synthesis route.

FTIR vibrational spectrum of LNP is shown in Figure 3(a) which reveals the presence of various functional groups. LNP showed three fundamental vibrations consisting of stretching modes [46]. Symmetric stretching appeared due to internal vibration of the P–O single bond at 971 cm^{−1}. Owing to the asymmetric stretching, a triplet has appeared in the region of the 1,055–1,150 cm^{−1}. The peak was observed, in the region between 400 and 700 cm^{−1} due to the transition metal ions. The peak at 646 cm^{−1} may also be due to asymmetric stretching vibrations of Ni–O bonds in the NiO₆ octahedron. WOR catalysis proceeds at NiO₆ edges of the metal oxides, and a high catalytic efficiency is perceived [47]. These observations suggested the presence of major functional groups related to Ni and (PO₄)^{3−}. Metal can accept diverse structures exhibiting different orientations of phosphate groups present in the crystal. Tunable coordination of PO₄[−] group can stabilize the transition state of metal by feasible modifications in its local positions; hence, a robust redox reaction can occur on the TM surface [48]. The vibrational spectra of LNCP-1, LNMP-2, and LP-3 are shown in Figure 3(b), and respective specific peaks are addressed in Table 3.

Employing cyclic voltammetry as the analytical tool, electroanalysis was performed with the potentials window of 0–1.6 V using 0.1 and 0.5 M potassium hydroxide as electrolyte and 0.05 M glucose as a sacrificial agent [49]. Conductive properties of synthesized samples are analyzed by using potassium ferricyanide and potassium chloride. Potassium ferricyanide has a known diffusion coefficient which provides information about catalytic performance. Voltammetric cycling for all modified electrodes was performed by employing 5 mM K₃[Fe(CN)₆] and 3 M KCl to estimate the active surface area of the modified electrodes [50,51]. The potential window for all modified electrodes to measure the surface area ranges from −0.2 to 1 as shown in Figure 4. A cyclic voltammogram for Fe²⁺/Fe³⁺ redox system depicts

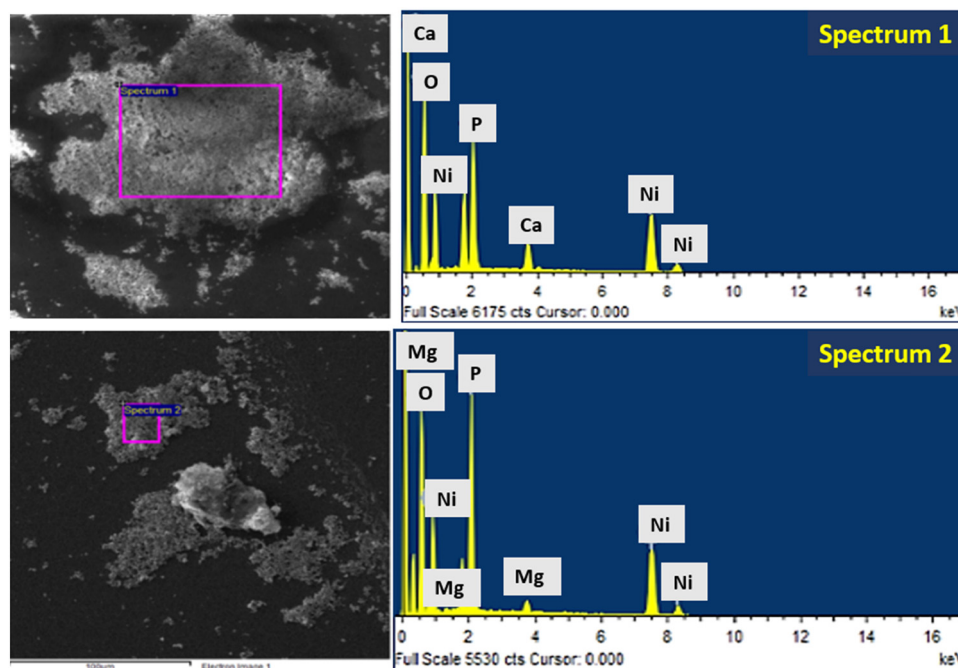


Figure 2: EDS spectra of LNCP-1 (spectrum 1) and LNMP-2 (spectrum 2).

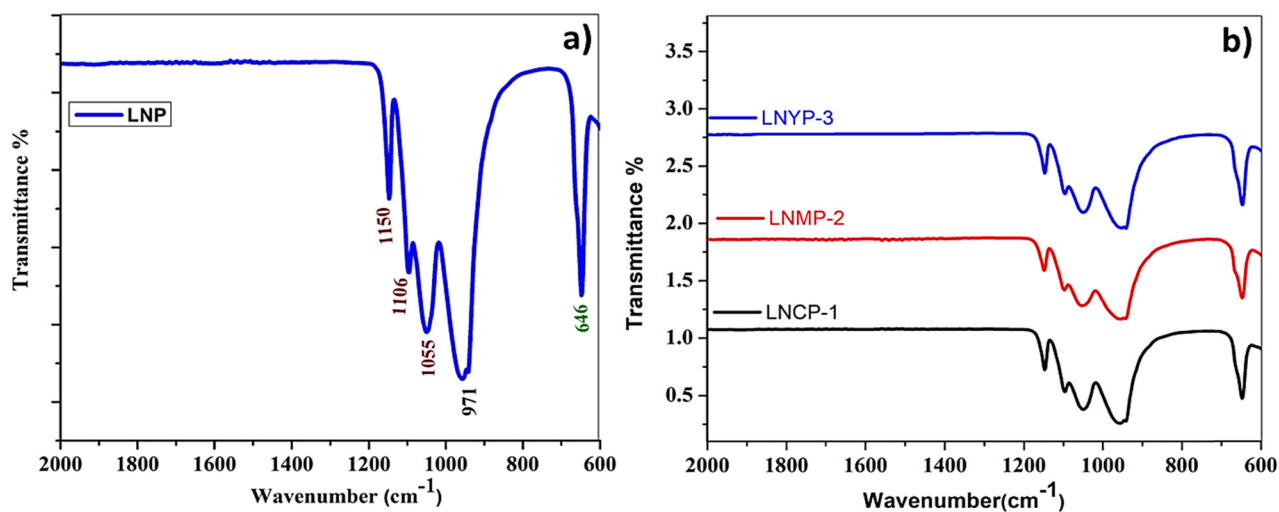


Figure 3: (a) FTIR spectrum of LNP; (b) FTIR spectrum of LNCP-1, LNMP-2 AND LNYP-3.

Table 3: Band assignment and wavenumber of FTIR spectra of LNP

Wave number (cm ⁻¹)	Assignment
646	M–O
971	$\nu_1(\text{PO}_4)^{3-}$
(1,056–1,150)	$\nu_3(\text{PO}_4)^{3-}$

the reversible electron transfer process. Corresponding to observed CV profiles showing a significant difference and

described that doping caused the enhancement in the electrical behavior. The Randles–Sevcik equation given by equation (2) was employed to evaluate the ECSA of fabricated electrodes [52].

$$I_{pa} = 2.69 \times 10^5 n^{3/2} AD^{1/2} \nu^{1/2} C, \quad (2)$$

where I_{pa} represents the anodic peak current of each catalyst in (μA), n indicates the number of electrons transferred (1 in this case), A shows the active surface area (cm^2), D denotes the diffusion coefficient ($0.76 \times 10^{-5} \text{ cm}^2 \text{ s}^{-1}$, 25°C),

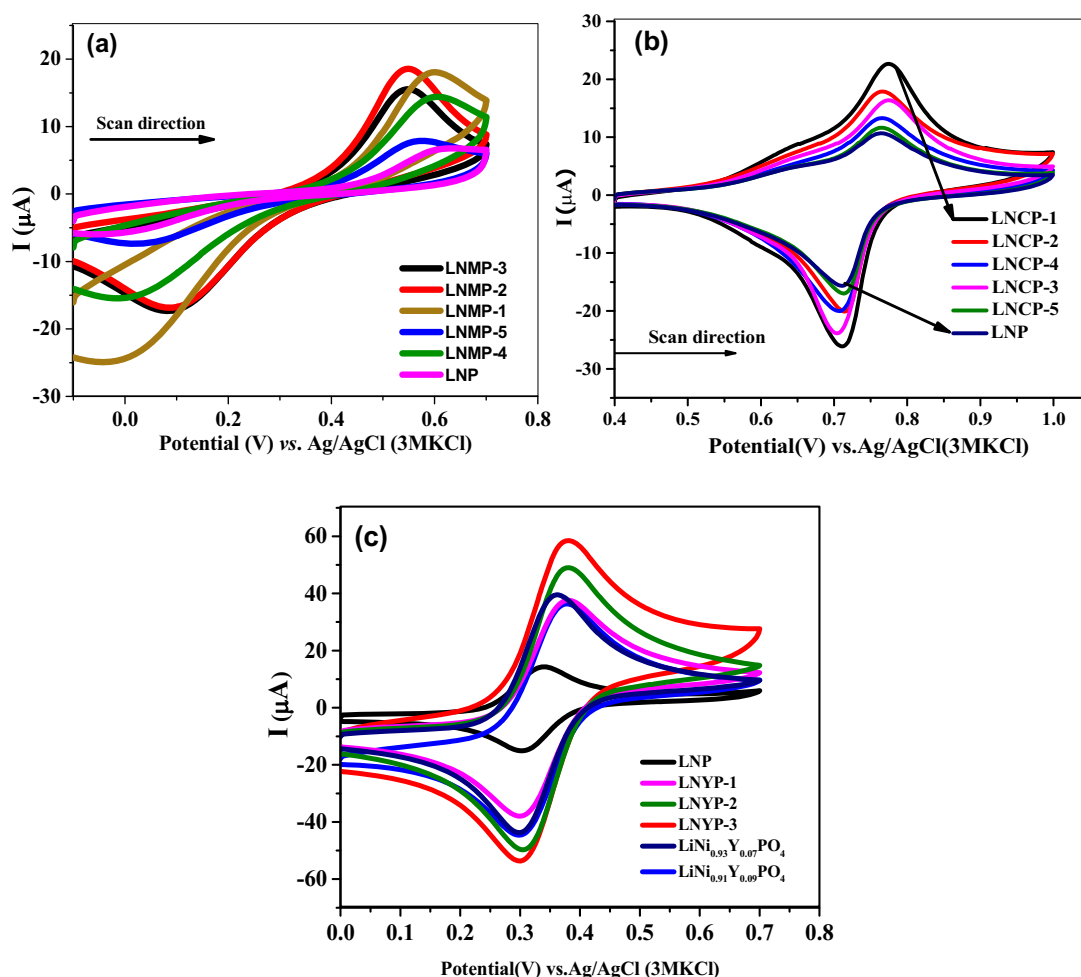


Figure 4: Cyclic voltammograms of synthesized samples in 5 mM $K_3[Fe(CN)_6]$ redox system (a) LNMP, (b) LNCP and (c) LNYP at 100 mV s^{-1} .

Table 4: Estimated active surface area for all synthesized samples

Samples	Active surface area (cm^2)	Samples	Active surface area (cm^2)
LNP	0.0005	LNCP-3	0.0011
LNMP-1	0.0015	LNCP-4	0.0013
LNMP-2	0.0016	LNCP-5	0.0010
LNMP-3	0.0012	LNYP-1	0.0032
LNMP-4	0.0011	LNYP-2	0.0041
LNMP-5	0.0006	LNYP-3	0.0050
LNCP-1	0.0018	LNYP-4	0.0034
LNCP-2	0.0015	LNYP-5	0.0030

v stands for scan rate (100 mV s^{-1}), and C is the analyte concentration (5 mM). Estimated ASA are listed in Table 4.

ECSA stands for the electrochemical surface area active for the reaction. The larger the ECSA exhibited by a catalytic material, a more facile reaction and boosted catalysis output is anticipated [50,53]. Values of active surface area range from

0.0012 to 0.0050 cm^2 . By comparing the value of the active surface area of metal ion-doped phosphate, it is deduced that a vivid difference exists between these series. From the calcium-doped series, LNCP-1 showed the highest value of ASA. From magnesium-doped series, LNMP-2 attained the maximum value of ASA. While in the yttrium-doped series, LNYP-3 depicted the highest value of ASA. The higher active surface area corresponds to the better catalytic activity of nanomaterials.

WOR has been studied by modifying the electrode with the samples at room temperature, and resultant cyclic voltammograms showed a single peak; *i.e.* only an anodic peak was observed. The electrocatalytic potential of lithium nickel phosphate and metal-doped LNP-fabricated GCE was determined using 0.1 and 0.5 M KOH as electrolyte and 0.05 M glucose between 0 and 1.6 V potential window, and an irreversible oxidation peak has been witnessed in the resultant voltammograms. CV profiles displayed in Figure 5 were recorded at fixed 100 mV s^{-1} for the various synthesized

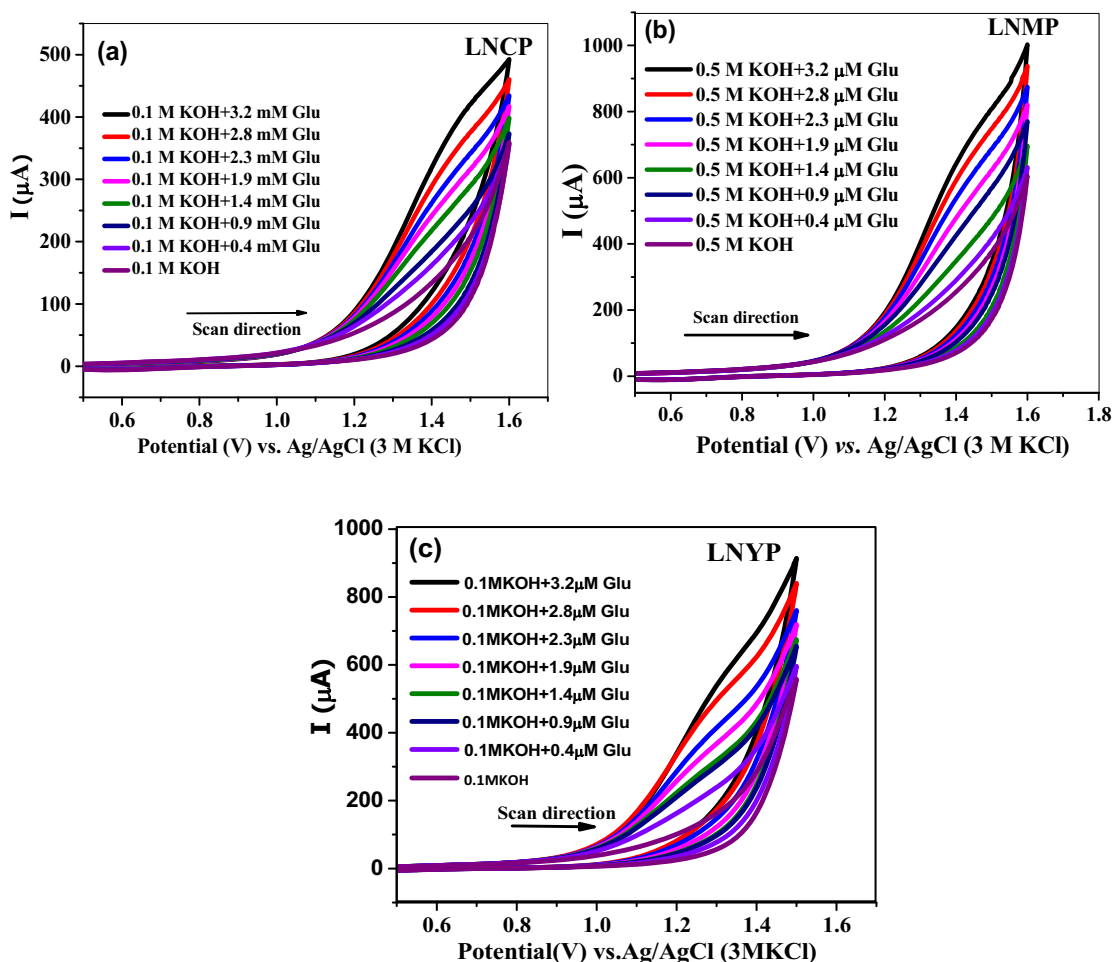


Figure 5: Cyclic voltammetric curves of LNCP-1-, LNMP-2-, and LNYP-3-modified electrode in 0.1 M KOH with different glucose concentrations at 100 mV s⁻¹.

materials. By adding different concentrations of glucose, the peak profiles showed an increase in the peak current of OER, which is the anodic half-reaction. As glucose concentration increases, the corresponding value of OER current increases indicating glucose-favored OER process [54]. Among all the series LNCP-1, LNMP-2, and LNYP-3 showed the highest peak current in their respective analogues. Reinmuth equation displayed by equation (3) was used to estimate the rate constants for the prepared materials [55]. Values of k^0 can be calculated from the slope by plotting a graph between I_p vs [glucose]. Values of the rate constant quantified the reversibility and irreversibility of the process going on the interface [56].

$$I_p = 0.227 nFAk^0, \quad (3)$$

where I_p is the anodic peak current in (A), F is Faraday's constant in (C/mole), A is an area of the electrode in (cm²), C is the concentration of glucose (mol cm³), and k^0 is the heterogeneous rate constant in (cm s⁻¹). The k^0 as shown in Table 5 for the WOR describes the capability of electron

transfer at the electrode–electrolyte interface and the reaction kinetics of the materials.

According to the values of the k^0 , the insulating and conductive behavior of the materials can be distinguished. The lowest value of k^0 thus indicates the insulating behavior of the LNP due to the slowest electrocatalytic property. The heterogeneous rate constant value for lithium nickel

Table 5: Calculated values of heterogeneous rate constant, diffusion, and mass transport coefficients

Sample	Heterogeneous rate constant k^0 (10^{-2} cm s ⁻¹)	Diffusion coefficient $D^0/10^{-5}$ (cm ² s ⁻¹)	Mass transport coefficient $m_T/10^{-3}$ (cm s ⁻¹)
LNP	1.1	0.3	0.8
LNCP-1	1.9	1.4	1.9
LNMP-2	3.9	5.2	3.6
LNYP-3	3.2	4.8	3.5

phosphate and metal ion-doped phosphate-modified GC electrode increased in the following order.

$$\text{LNP} < \text{LNCP} - 1 < \text{LNYP} - 3 < \text{LNMP} - 2$$

Doping of magnesium resulted in the highest value of the rate constant which proved it to be a good scheme of the catalysts.

The electroactivity of synthesized material was tested using cyclic voltammetry in the presence of 0.5 M KOH and 0.7 ml of glucose (facilitating agent), which equates to 0.05 molarity of glucose. The scan rate was varied from 20 to 100 mV s^{-1} within the potential window (0–0.5, and 1.6 V) at room temperature. The CV responses of LNCP-1, LNMP-2, and LNYP-3 for OER are presented in Figure 6. Voltammograms for OER using various synthesized samples at different scan rates showed the responsive increase in the peak current gradually as the scan rate was varied from 20 to 100 mV s^{-1} . It was also inferred that the electroactivity

of the synthesized material was better in the presence of 0.05 M glucose than that in KOH solution only. Analyzing the overall voltammetric profiles for all samples, LNCP-1, LNMP-2, and LNMP-3 showed the best results from all doped LNP analogues.

Furthermore, to enhance the understanding of the electrocatalytic potential of LNMPs, the diffusion coefficient “ D^0 ” was calculated using the Randles-Sevcik equation for irreversible processes. Electrocatalytic property of the materials gives information on facile electron transfer process by the electrochemical response. By using the equation (4), the mass transport coefficient is calculated [57].

$$m_T = [D^0(RT/Fv)]^{1/2}. \quad (4)$$

Mass transport coefficient tells the electron transferability of the analyte. The kinetics of redox reactions occurring at the electrode-analyte contact are determined by the m_T value. The values of D^0 and m_T are a clear indication of

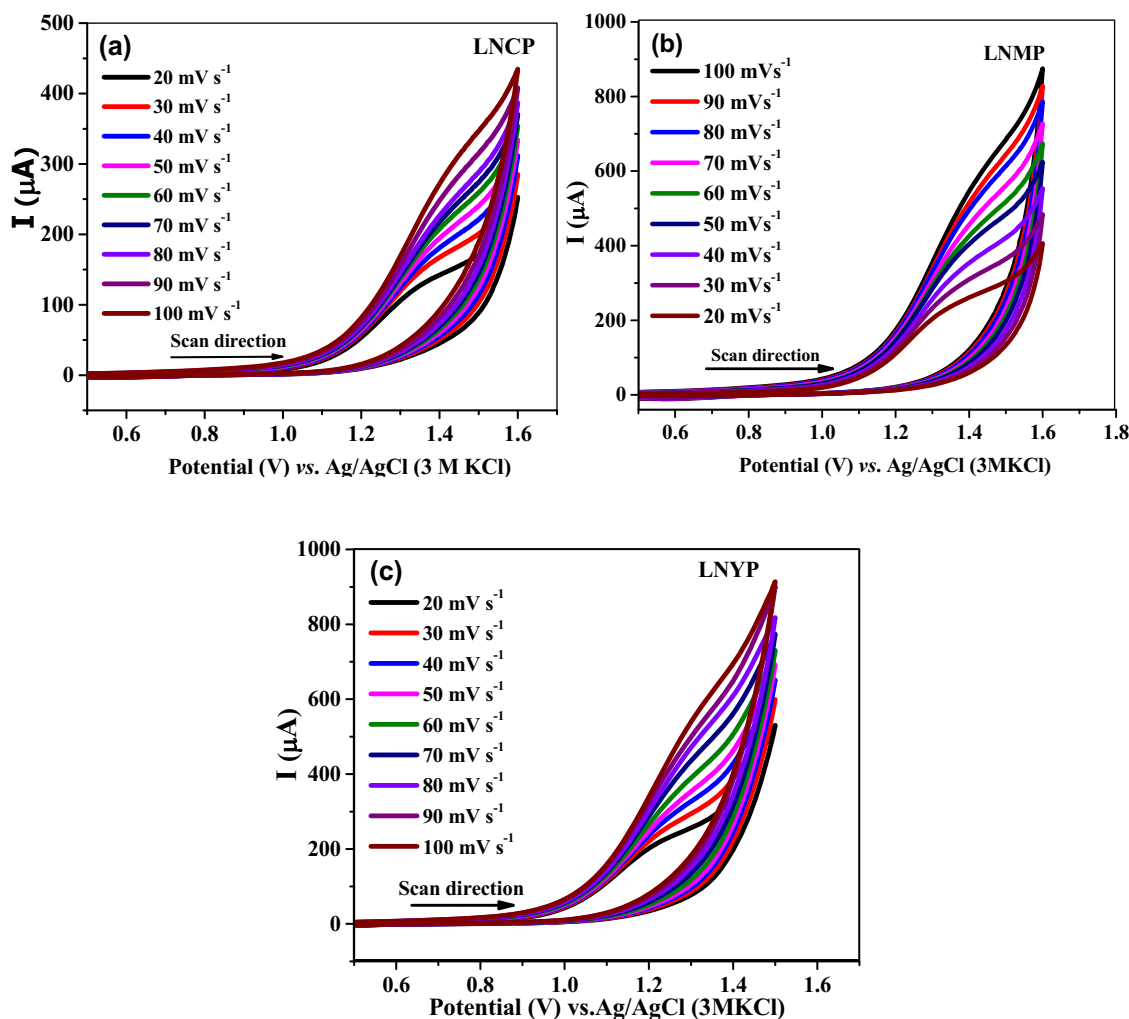


Figure 6: Cyclic voltammetric responses at LNC1-, LNMP-2-, and LNYP-3-modified electrode in 0.5 M KOH + 3.27 μM glucose at 20–100 mV s^{-1} .

the irreversible nature of the electrode process and the smallest for LNP, indicating it to be less efficient for OER electrocatalysis. The trend for the optimized samples is as follows:

$$\text{LNP} < \text{LNCP-1} < \text{LNYP-3} < \text{LNMP-2}$$

Magnesium doping shows an increase in the value of the D^0 due to the fast electron transfer process. LNMP-2 shows the highest values of both D^0 and k^0 , which indicates these materials to be the better catalyst as compared to the other prepared samples.

To analyze the effect of the temperature on the electroactivity of the prepared pure lithium nickel phosphate catalyst and its doped analogues, the temperature was varied from 20 to 40°C at 100 mV s⁻¹ scan rate in 0.5 M KOH in the presence of 3.27 μM optimal glucose concentration, and the CV responses were observed for each composition. At elevated temperatures, the kinetics of water-splitting was facilitated, and Figure 7 shows the enhancement in the

current by increasing the temperature for three optimized samples.

By increasing the temperature, active sites of the electrode are free from the adsorbed CO, due to this reason high temperature is required for the water oxidation for such materials. The maximum current was observed for the LNMP-2 composition, *i.e.* 1.33 mA for water oxidation at 40°C.

To calculate the thermodynamic parameters, the Marcus equation (equation (5)) is used [58].

$$k_s = Z_{\text{het}} \exp[-\Delta G/RT]. \quad (5)$$

A more simplified form of the Marcus equation is given in equation (6).

$$\ln(k_s/Z_{\text{het}}) = -\Delta H^*/RT + \Delta S^*/R, \quad (6)$$

where Z_{het} is the collision frequency and can be calculated at any temperature with the help of the following relation shown in equation (7).

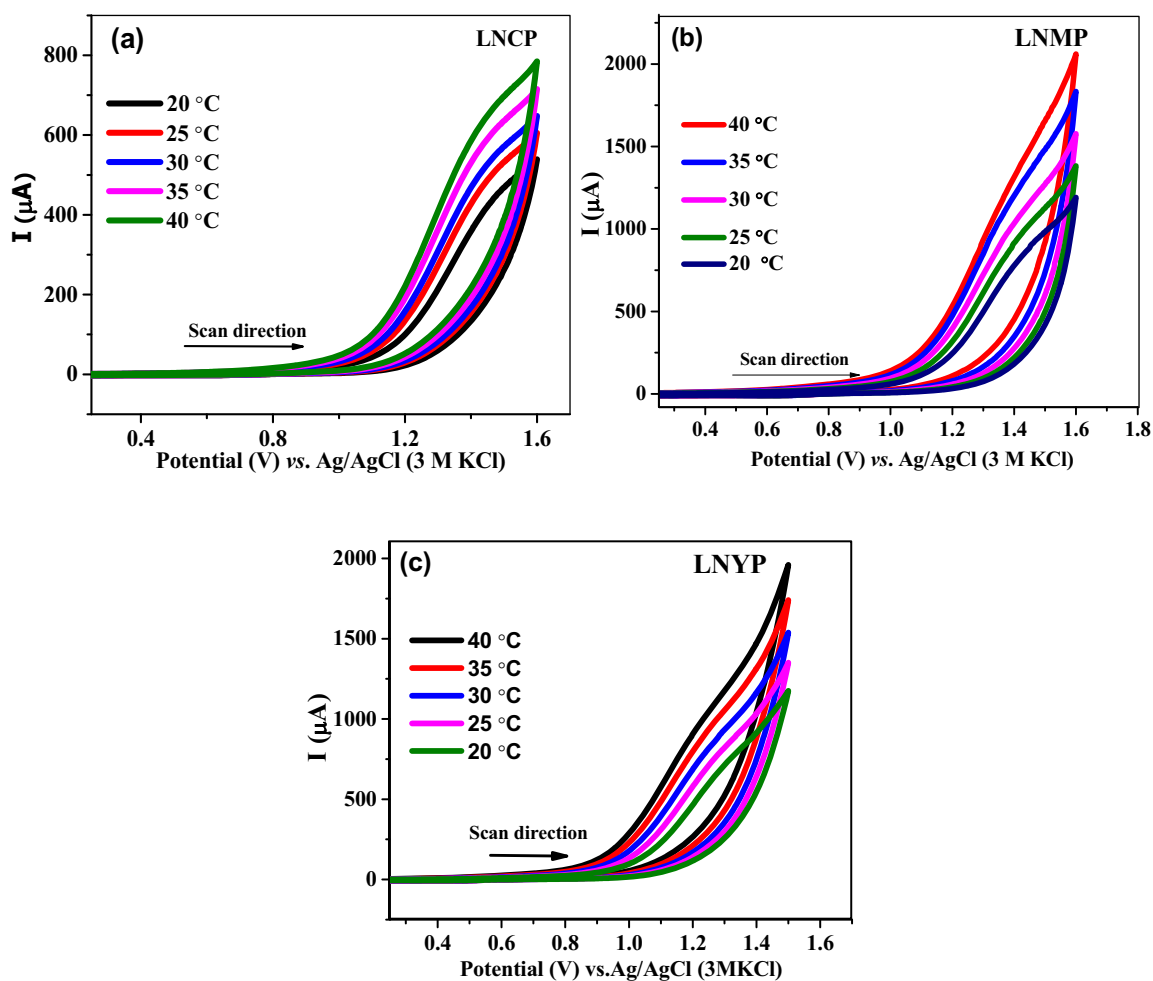


Figure 7: Cyclic voltammetric responses of LNCP-1, LNMP-2, and LNYP-3 in 0.1 M KOH + 3.2 μM glucose at 20–40°C and 100 mV s⁻¹ scan rate.

$$Z_{\text{het}} = (RT/2\pi M)1/2, \quad (7)$$

where M is the molar mass of glucose and G is the Gibbs free energy.

Respective ΔH^* and ΔS^* values were obtained from the slope and the intercept of the Marques Equation plots. ΔH^* and ΔS^* values were retrieved by plotting the graphs between the $\ln(k_s/Z_{\text{het}})$ vs $1/T$. The values of activation energies were calculated by using the following relation in equation (8).

$$\Delta G^* = \Delta H^* - T\Delta S^*. \quad (8)$$

where ΔH^* and ΔG^* showed a positive value, which specifies that water oxidation in the presence of glucose is an activation-controlled process. Also, the reaction is endothermic in nature, and the spontaneous flow of the reaction takes place in forward direction [59]. Hence, on operating the electrochemical cells at higher temperatures, the functions of electrocatalysts are effectively improved due to an increase in the catalytic activities. Minimum value of activation energy as observed in Table 6 was observed for the $\text{LiNi}_{0.97}\text{Mg}_{0.03}\text{PO}_4$ (LNMP-2) composition; therefore, it is suggested as the best electrocatalyst among all other analogues.

Furthermore, different groups of compounds have been employed as water oxidation electrocatalysts. A comparative analysis presented in Table 7 with electrochemical parameters indicate that the presented LNMP-based composites are superior catalysts for WOR owing to the developed electronic and transport properties of the materials. In this way, particularly effective and firm WOR electrocatalysts

are anticipated for future energy bids. Increase in number of active sites by tuning the structure of the electrocatalyst and enhancement in inherent activity of active sites by modifying their atomic and electronic states. Such flexibility of LMNPs makes them available as proficient catalysts for future electronic devices [60].

4 Conclusions

In this study, the non-aqueous sol-gel method was used to successfully synthesize the single-phase LNP and doped LNMP nanoparticles calcined at 850°C in an air atmosphere. XRD for pristine LNP and magnesium doped LNP patterns with intact phases according to the peak analysis ensured the stability of the material. Single-phase orthorhombic crystalline structure was obtained for LNP and magnesium doped analogs, suggesting the appropriateness of doping into the crystal lattice of lithium nickel phosphate. Average crystallite sizes determined using XRD were found to lie in the 7–10 nm range. FTIR spectra indicated the corresponding peaks of phosphate ion and metal oxide in lithium nickel oxide. No extra band appeared in the doped analogs thus conforming to the purity of synthesized samples. SEM micrographs showed nanoparticles to be nearly spherical in shape with a homogeneous distribution of particles. The EDX results showed that the stoichiometric amount of magnesium added was in good agreement with the theoretical values. The maximum ASA and the highest peak current were associated with LNMP-2 composition. All materials showed potential applications in the WOR catalysis and electrocatalysis the oxygen evolution reaction in 0.5 M KOH and glucose. In a basic medium, all the prepared samples responded to water oxidation, but LNMP-2 produced the best results, with the highest D^0 ($5.2 \times 10^{-5} \text{ cm}^2 \text{ s}^{-1}$) and k^0 value ($3.2 \times 10^{-2} \text{ cm s}^{-1}$) for WOR. $\text{LiNi}_{0.95}\text{Y}_{0.05}\text{PO}_4$ i.e. LNYP-3 is found to be the optimum catalyst among its series. For LNMP-2, the high peak current value and low onset potential (0.90 V vs Ag/AgCl) demonstrated the catalyst's potential for the water oxidation reaction. In conclusion, all electrocatalysts have a strong electrocatalytic potential for WOR and high-performance DMFCs. The synthesized catalysts can be recommended as promising candidates for further electroanalytical research.

Funding information: The experimental work has been accomplished at Fuel Cell Lab, Department of Chemistry, QAU, Islamabad. This work was funded by the Researchers Supporting Project Number (RSP2024R441), King Saud University, Riyadh, Saudi Arabia. We are highly thankful

Table 6: Thermodynamic parameters of LNP and its doped series in 0.5 M KOH + 3.27 μM glucose at 100 mV s^{-1} scan rate and 20–40°C

Samples	ΔG (kJ mol^{-1})	ΔH (kJ mol^{-1})
LNP	26.8	18.2
LNCP-1	24.4	12.1
LNMP-2	23.1	14.0
LNYP-3	23.6	10.5

Table 7: Literature comparison with recently reported catalysts for WOR

Catalysts	D^0 ($\text{cm}^2 \text{ s}^{-1}$)	k^0 (cm s^{-1})	Ref.
$\text{Ag}_2\text{O}/\gamma\text{-Al}_2\text{O}_3$	6.5×10^{-6}	2.4×10^{-4}	[61]
$(\text{Fe, Al, Mg, Cd, Cr, Mn})_3\text{O}_4$	2.74×10^{-8}	3.04×10^{-4}	[31]
$(\text{Fe, Al, Mg, Cu, Ni, Co})_3\text{O}_4$	9.31×10^{-8}	7.05×10^{-4}	[31]
$\text{Ag}_2\text{O}-\text{PrO}_2/\gamma\text{-Al}_2\text{O}_3$	1.92×10^{-6}	7.40×10^{-3}	[62]
LNCP-1	1.9×10^{-5}	1.4×10^{-2}	This work
LNMP-2	3.9×10^{-5}	5.2×10^{-2}	This work
LNYP-3	3.2×10^{-5}	4.8×10^{-2}	This work

to HEC Pakistan for Project 2014 4768 for the Gamry instrument.

Author contributions: Synthesis and electrochemical studies: Mehwish Huma Nasir, Hajra Niaz, Naila Yunus, and Urooj Ali; manuscript preparation: Safia Khan and Tehmeena Maryum Butt; data analysis: Mehwish Huma Nasir; Manuscript proofreading/editing: Hina Naeem, Hu Li and Mohamed A. Habila; Supervision: Naveed Kausar Janjua. All authors have accepted responsibility for the entire content of this manuscript and approved its submission.

Conflict of interest: The authors state no conflict of interest.

References

- [1] Rehman A, Ulucak R, Murshed M, Ma H, Işık C. Carbonization and atmospheric pollution in China: The asymmetric impacts of forests, livestock production, and economic progress on CO₂ emissions. *J Environ Manag.* 2021;294:113059.
- [2] Zhou Y, Li R, Lv Z, Liu J, Zhou H, Xu C. Green hydrogen: A promising way to the carbon-free society. *Chin J Chem Eng.* 2022;43:2–13.
- [3] Paska J, Surma T. Electricity generation from renewable energy sources in Poland. *Renew Energy.* 2014;71:286–94.
- [4] Tan H, Li J, He M, Li J, Zhi D, Qin F, et al. Global evolution of research on green energy and environmental technologies: A bibliometric study. *J Environ Manag.* 2021;297:113382.
- [5] Oncel SS. Green energy engineering: Opening a green way for the future. *J Clean Prod.* 2017;142:3095–100.
- [6] Diffenbaugh NS, Burke M. Global warming has increased global economic inequality. *Proc Natl Acad Sci.* 2019;116:9808–13.
- [7] McLaren JA, Mullendore S, Laws ND, Anderson KH. Valuing the resilience provided by solar and battery energy storage systems. *National Renewable Energy Lab. (NREL);* 2018.
- [8] Fang Y-H, Liu Z-P. Mechanism and tafel lines of electro-oxidation of water to oxygen on RuO₂ (110). *J Am Chem Soc.* 2010;132:18214–22.
- [9] Braunschweig B, Hibbitts D, Neurock M, Wieckowski A. Electrocatalysis: A direct alcohol fuel cell and surface science perspective. *Catal Today.* 2013;202:197–209.
- [10] Wieckowski A, Neurock M. Contrast and synergy between electrocatalysis and heterogeneous catalysis. *Adv Phys Chem.* 2011;11:1–11.
- [11] Shen L, Ying J, Ozoemena KI, Janiak C, Yang XY. Confinement effects in individual carbon encapsulated nonprecious metal-based electrocatalysts. *Adv Funct Mater.* 2022;32:2110851.
- [12] Kim J-S, Han JW, Lee B-J. Alloying non-precious metals into Ni-based electrocatalysts for enhanced hydrogen oxidation reaction in alkaline media: A computational study. *Appl Surf Sci.* 2021;554:149627.
- [13] Chen F, Sun Y, Li H, Li C. Review and development of anode electrocatalyst carriers for direct methanol fuel cell. *Energy Technol.* 2022;10:2101086.
- [14] Chai Z, Zhang C, Wang H, Bi X, Bai P, Wang X. Increased interface effects of PtFe alloy/CeO₂/C with PtFe selective loading on CeO₂ for superior performance in direct methanol fuel cell. *Int J Hydrog Energy.* 2019;44:4794–808.
- [15] Vecchio CL, Lyu X, Gatto I, Zulevi B, Serov A, Baglio V. Performance investigation of alkaline direct methanol fuel cell with commercial PGM-free cathodic materials. *J Power Sources.* 2023;561:232732.
- [16] Mehrotra S, Kumar VK, Gajalakshmi S, Pathak B. Bioelectrogenesis from ceramic membrane-based algal-microbial fuel cells treating dairy industry wastewater. *Sustain Energy Technol Assess.* 2021;48:101653.
- [17] Lide DR. *CRC handbook of chemistry and physics.* USA: CRC Press; 2004.
- [18] Kim U, Lee S, Koo D, Choi Y, Kim H, Son E, et al. Crystal facet and electronic structure modulation of perovskite oxides for water oxidation. *ACS Energy Lett.* 2023;8:1575–83.
- [19] Ateia EE, AL-Hamzi A, Hussein B. Synthesis and characterization of non-stoichiometric cobalt nanoferrites for multifunctional applications. *J Mater Sci: Mater Electron.* 2022;33:20642–55.
- [20] Oliveira LC, Venâncio R, de Azevedo PV, Anchieta CG, Nepel TC, Rodella CB, et al. Reviewing perovskite oxide sites influence on electrocatalytic reactions for high energy density devices. *J Energy Chem.* 2023;81:1–19.
- [21] Yu J, Cao Q, Li Y, Long X, Yang S, Clark JK, et al. Defect-rich NiCeO_x electrocatalyst with ultrahigh stability and low overpotential for water oxidation. *ACS Catal.* 2019;9:1605–11.
- [22] Liu Y, Han Y, Zhang Z, Zhang W, Lai W, Wang Y, et al. Low overpotential water oxidation at neutral pH catalyzed by a copper (II) porphyrin. *Chem Sci.* 2019;10:2613–22.
- [23] Lei Z, Wang T, Zhao B, Cai W, Liu Y, Jiao S, et al. Recent progress in electrocatalysts for acidic water oxidation. *Adv Energy Mater.* 2020;10:2000478.
- [24] Angeles-Olvera Z, Crespo-Yapur A, Rodríguez O, Cholula-Díaz JL, Martínez LM, Videa M. Nickel-based electrocatalysts for water electrolysis. *Energies.* 2022;15:1609.
- [25] Liu X, Wang X, Yuan X, Dong W, Huang F. Rational composition and structural design of in situ grown nickel-based electrocatalysts for efficient water electrolysis. *J Mater Chem A.* 2016;4:167–72.
- [26] Mauger A, Julien CM. Olivine positive electrodes for Li-ion batteries: Status and perspectives. *Batteries.* 2018;4:39.
- [27] Boyadzhieva T, Koleva V, Stoyanova R. Crystal chemistry of Mg substitution in NaMnPO₄ olivine: concentration limit and cation distribution. *Phys Chem Chem Phys.* 2017;19:12730–9.
- [28] Gershinsky Y, Zysler M, Shokhen V, Stone Y, Zitoun D. Dual alkaline ion route to chemical de-insertion in oxygen evolution olivine electrocatalysts. *ACS Catal.* 2019;9:8355–63.
- [29] Janjua NK, Mumtaz M, Yaqub A, Sabahat S, Mujtaba A. Electrocatalytic activity of LiNiPO₄ and the copper doped analogues towards oxygen reduction. *Nucl.* 2014;51:109–15.
- [30] Indra A, Menezes PW, Schwarze M, Driess M. Visible light driven non-sacrificial water oxidation and dye degradation with silver phosphates: multi-faceted morphology matters. *New J Chem.* 2014;38:1942–5.
- [31] Asim M, Hussain A, Khan S, Arshad J, Butt TM, Hana A, et al. Sol-gel synthesized high entropy metal oxides as high-performance catalysts for electrochemical water oxidation. *Molecules.* 2022;27:5951.
- [32] Kumaravel V, Imam MD, Badreldin A, Chava RK, Do JY, Kang M, et al. Photocatalytic hydrogen production: role of sacrificial reagents on the activity of oxide, carbon, and sulfide catalysts. *Catalysts.* 2019;9:276.

- [33] Lakhera SK, Rajan A, Rugma T, Bernaurdshaw N. A review on particulate photocatalytic hydrogen production system: Progress made in achieving high energy conversion efficiency and key challenges ahead. *Renew Sustain Energy Rev.* 2021;152:11694.
- [34] Ren P, Zhang T, Jain N, Ching HV, Jaworski A, Barcaro G, et al. An atomically dispersed Mn-photocatalyst for generating hydrogen peroxide from seawater via the water oxidation reaction (WOR). *J Am Chem Soc.* 2023;145(30):16584–96.
- [35] Priyadharsini N, Kasturi PR, Shanmugavani A, Surendran S, Shanmugapriya S, Selvan RK. Effect of chelating agent on the sol-gel thermolysis synthesis of LiNiPO_4 and its electrochemical properties for hybrid capacitors. *J Phys Chem Solids.* 2018;119:183–92.
- [36] Mumtaz M, Janjua NK, Yaqub A, Sabahat S. Microwave assisted non-aqueous sol–gel synthesis of LiNiPO_4 and its copper doped analogues. *J Sol-Gel Sci Technol.* 2014;72:56–62.
- [37] Ahmad A, Khan S, Tariq S, Luque R, Verpoort F. Self-sacrifice MOFs for heterogeneous catalysis: Synthesis mechanisms and future perspectives. *Mater Today.* 2022;55:137–69.
- [38] Wu Q, Sang S, Wang G, Wang Q, Huang L, Zhu T, et al. Enhanced near-and mid-infrared radiation property of MgCr_2O_4 by doping with Cu ions. *Ceram Int.* 2023;49:17008–17.
- [39] Mahmoud AED, Stolle A, Stelter M. Sustainable synthesis of high-surface-area graphite oxide via dry ball milling. *ACS Sustain Chem Eng.* 2018;6:6358–69.
- [40] Nasir MH, Janjua NK, Santoki J. Electrochemical performance of carbon modified LiNiPO_4 as Li-ion battery cathode: A combined experimental and theoretical study. *J Electrochem Soc.* 2020;167:130526.
- [41] Enayati M, Aryanpour G, Ebnonnasir A. Production of nanostructured WC–Co powder by ball milling. *Int J Refract Met Hard Mater.* 2009;27:159–63.
- [42] Peterson SC, Jackson MA, Kim S, Palmquist DE. Increasing biochar surface area: Optimization of ball milling parameters. *Powder Technol.* 2012;228:115–20.
- [43] Khan S, Shah SS, Yurtcan AB, Bahajaj AAA, Zafar A, Janjua NK. Electrooxidation of ammonia at high-efficiency $\text{RuO}_2\text{-ZnO}/\text{Al}_2\text{O}_3$ and $\text{PdO-ZnO}/\text{Al}_2\text{O}_3$ mesoporous catalysts; an innovative strategy towards clean fuel technology. *Fuel.* 2023;347:128446.
- [44] Tao Y, Zhu B. Yttrium ion doping effect on electrochemical performance of LiNiPO_4 materials. *Ionics.* 2021;27:2909–14.
- [45] Hulbert BS, Kriven WM. Specimen-displacement correction for powder X-ray diffraction in Debye–Scherrer geometry with a flat area detector. *J Appl Crystallogr.* 2023;56:160–6.
- [46] Salah AA, Jozwiak P, Garbarczyk J, Benkhoucha K, Zaghbi K, Gendron F, et al. Local structure and redox energies of lithium phosphates with olivine-and Nasicon-like structures. *J Power Sources.* 2005;140:370–5.
- [47] Yoshida M, Mitsutomi Y, Mineo T, Nagasaka M, Yuzawa H, Kosugi N, et al. Direct observation of active nickel oxide cluster in nickel–borate electrocatalyst for water oxidation by in situ O K-edge X-ray absorption spectroscopy. *J Phys Chem C.* 2015;119:19279–86.
- [48] Kim H, Park J, Park I, Jin K, Jerng SE, Kim SH, et al. Coordination tuning of cobalt phosphates towards efficient water oxidation catalyst. *Nat Commun.* 2015;6:8253.
- [49] Wang Y, Yan W, Ni M, Zhu C, Du H. Surface valence regulation of cobalt–nickel foams for glucose oxidation-assisted water electrolysis. *Chem Commun.* 2023;59:2485–8.
- [50] Khan S, Shah SS, Anjum MAR, Khan MR, Janjua NK. Electro-oxidation of ammonia over copper oxide impregnated $\gamma\text{-Al}_2\text{O}_3$ nanocatalysts. *Coatings.* 2021;11:313.
- [51] Khan S, Shah SS, Ahmad A, Yurtcan AB, Jabeen E, Alshgari RA, et al. Ruthenium and palladium oxide promoted zinc oxide nanoparticles: Efficient electrocatalysts for hydrazine oxidation reaction. *J Electroanal Chem.* 2022;917:116422.
- [52] Hamzah IH, Abd Manaf A, Sidek O. A study on characteristic and reliability of fabricated microfluidic three electrodes sensor based on Randle-Sevcik equation. 2010 IEEE Asia Pacific Conference on Circuits and Systems. IEEE; 2010. p. 816–9.
- [53] Khan S, Shah SS, Ahmad A, Yurtcan AB, Katubi KM, Janjua NK. γ -Alumina supported copper oxide nanostructures promoted with ruthenium oxide ($\text{RuO}_2\text{-CuO}/\text{Al}_2\text{O}_3$) and palladium oxide ($\text{PdO-CuO}/\text{Al}_2\text{O}_3$): Efficient electrodes for heterogeneous catalysis of ammonia electrooxidation. *J Electrochem Soc.* 2022;169:076512.
- [54] Wang W, Zhang L, Tong S, Li X, Song W. Three-dimensional network films of electrospun copper oxide nanofibers for glucose determination. *Biosens Bioelectron.* 2009;25:708–14.
- [55] Janjua NK, Jabeen M, Islam M, Yaqub A, Sabahat S, Mehmood S, et al. Electrochemical properties of barium cerate doped with zinc for methanol oxidation. *J Chem Soc Pak.* 2015;37:11–26.
- [56] Butt TM, Erum S, Mujtaba A, Medvedev D, Janjua NK. Nickel-doped lanthanum cerate nanomaterials as highly active electrocatalysts. *Front Chem.* 2022;10:1064906.
- [57] Parthasarathy A, Srinivasan S, Appleby AJ, Martin CR. Pressure dependence of the oxygen reduction reaction at the platinum microelectrode/naion interface: electrode kinetics and mass transport. *J Electrochem Soc.* 1992;139:2856.
- [58] Khan ASA, Ahmed R, Mirza ML. Comparison of catalytic activities of carbon supported Pt and Pt-Ru catalysts for methanol oxidation in neutral and basic media by cyclic voltammetry. *Turk J Chem.* 2008;32:743–53.
- [59] Khan ASA. Evaluation of thermodynamic parameters of cadmium adsorption on sand from Temkin adsorption isotherm. *Turk J Chem.* 2012;36:437–43.
- [60] Guo T, Li L, Wang Z. Recent development and future perspectives of amorphous transition metal-based electrocatalysts for oxygen evolution reaction. *Adv Energy Mater.* 2022;12:2200827.
- [61] Butt TM, Ullah A, Janjua NKJ. Electrokinetic analysis of water oxidation on alumina supported silver oxide nanopowders. *J Electroanal Chem.* 2022;907:116053.
- [62] Khan M, Janjua NK, Ahmad A, Luque R, Al-Kahtani AA, Tighezza AM. Highly effective bi-functional electrochemical activity of $\text{Ag}_2\text{O-PrO}_2/\gamma\text{-Al}_2\text{O}_3$ electrocatalysts towards OER and ORR. *Int J Energy Res.* 2022;46:14161–73.